Frontiers in Bioscience Landmark

Front. Biosci. (Landmark Ed) **2023**; 28(10): 249
https://doi.org/10.31083/j.fbl2810249

Original Research

Rapid Detection and Analysis of Raman Spectra of Bacteria in Multiple Fields of View Based on Image Stitching Technique

Xiaohui Dou[1,†], Fengna Yang[1,†], Nan Wang[2], Ying Xue[2], Haoran Hu[1], Bei Li[1,2,3,*]

[1]Department of Biomedical Engineering, Wenzhou Medical University, 325035 Wenzhou, Zhejiang, China
[2]Department of Research and Development, Hooke Instruments, 130033 Changchun, Jilin, China
[3]Key Laboratory of Optical System Advanced Manufacturing Technology, Changchun Institute of Optics, Fine Mechanics and Physics, Chinese Academy of Sciences, 130033 Changchun, Jilin, China
*Correspondence: beili@ciomp.ac.cn (Bei Li)
[†]These authors contributed equally.
Academic Editor: Josef Jampílek
Submitted: 30 December 2022 Revised: 17 April 2023 Accepted: 14 June 2023 Published: 19 October 2023

Abstract

Background: Due to antibiotic abuse, the problem of bacterial resistance is becoming increasingly serious, and rapid detection of bacterial resistance has become an urgent issue. Because under the action of antibiotics, different active bacteria have different metabolism of heavy water, antibiotic resistance of bacteria can be identified according to the existence of a C-D peak in the 2030–2400 cm^{-1} range in the Raman spectrum. **Methods**: To ensure data veracity, a large number of bacteria need to be detected, however, due to the limitation of the field of view of the high magnification objective, the number of single cells in a single field of view is very small. By combining an image stitching algorithm, image recognition algorithm, and processing of Raman spectrum and peak-seeking algorithm, can identify and locate single cells in multiple fields of view at one time and can discriminate whether they are Antimicrobial-resistant bacteria. **Results**: In experiments 1 and 2, 2706 bacteria in 9 × 11 fields of view and 2048 bacteria in 11 × 11 fields of view were detected. Results showed that in experiment 1, there are 1137 antibiotic-resistant bacteria, accounting for 42%, and 1569 sensitive bacteria, accounting for 58%. In experiment 2, there are 1087 antibiotic-resistant bacteria, accounting for 53%, and 961 sensitive bacteria, accounting for 47%. It showed excellent performance in terms of speed and recognition accuracy as compared to traditional manual detection approaches. And solves the problems of low accuracy of data, a large number of manual experiments, and low efficiency due to the small number of single cells in the high magnification field of view and different peak-seeking parameters of different Raman spectra. **Conclusions**: The detection and analysis method of bacterial Raman spectra based on image stitching can be used for unattended, automatic, rapid and accurate detection of single cells at high magnification with multiple fields of view. With the characteristics of automatic, high-throughput, rapid, and accurate identification, it can be used as an unattended, universal and non-invasive means to measure antibiotic-resistant bacteria to screen for effective antibiotics, which is of great importance for studying the persistence and spread of antibiotics in bacterial pathogens.

Keywords: image stitching; Raman spectrum; image recognition; antibiotic resistance; multiple fields of view; heavy water labeling

1. Introduction

The first discovery of antibiotics was in 1982, which was an outstanding milestone in the history of antibiotic development. However, the overuse of antibiotics has produced bacteria resistant to multiple antibiotics [1,2]. The emergence of antibiotic resistance in bacteria has caused a great deal of public health concern [3]. An analysis of the global burden of antimicrobial resistance found that in 2019, resistant bacteria were responsible for 4.95 million deaths, of which 1.25 million were directly due to resistance [4]. Human health is at great risk due to the massive spread of antibiotic resistance [5,6]. Therefore, it is necessary to obtain an ultrasensitive and rapid way to detect bacterial antibiotic resistance [7–9], which is of great significance for protecting human health.

In 1928, Indian scientist C.V. Raman discovered the Raman scattering effect. Since the molecular vibrations of different substances are different, the Raman spectrometer can absorb Raman scattered light to form a spectrum, thereby providing the "fingerprint" of the substance, that is, analyzing the biological information of the substance through the Raman spectroscopy system [10]. In contrast to traditional single-cell analysis methods, Raman spectroscopy has the characteristics of using less sample, rapid analysis, and no injury to cells [11,12]. Using single-cell Raman spectroscopy to detect the vibrational modes of biomolecules in cells can reflect biochemical characteristics or phenotypes at the single-cell level. Cells exhibit characteristic Raman spectral shifts due to the replacement of isotope atoms with molecules of matter [6]. Detection of single-cell activity is key to the study of cellular antibiotic resistance. Raman spectroscopy now has proven applications in the fields such as microbial classification and analysis of cellular drug resistance [13,14]. In recent years, the heavy water (D_2O) labeling method has been proposed to substitute traditional isotopic methods for the detection of single-cell activity [15]. The incorporation of heavy

water allows the identification of active cells in the sample while avoiding biases due to the introduction of carbon or nitrogen. Cells containing C-D bonds display distinguishable Raman bands (2030–2400 cm^{-1}), shifted approximately 3000 cm^{-1} from C-H vibrations that can serve as unique biomarkers of the metabolic activity of individual cells, while under the action of antibiotics to inhibit the metabolism of cells, susceptible bacteria will not display this band [6]. Antibiotic-resistant bacteria will continue to metabolize deuterium in heavy water under the action of antibiotics. Microscopic Raman spectroscopy can detect biomacromolecules containing carbon-deuterium chemical bonds synthesized in cells after bacteria metabolize deuterium, thus enabling culture-independent rapid antibiotic sensitivity detection at the single-cell level [16,17]. Therefore, single-cell D_2O-Raman provides a good approach to combat antibiotic resistance by revealing the metabolic activity of metabolically active cells to antibiotics, regardless of their culture capacity [18].

To avoid contingency, the more bacterial Raman spectra analyzed when measuring antibiotic-resistant bacteria, the more accurate and reliable the experimental conclusions. The method researched in this paper focuses on single-cell Raman spectra. However, after a certain dilution, there are still exist impurities and cluster phenomena in microbial samples. Since the traditional Raman acquisition method scans through small fields of view one by one and there are impurities, cluster phenomena, and too few single cells in a single small field of view, it is necessary to manually screen the single cell in a single field of view and it is not feasible to automate the acquisition of a large number of bacterial Raman spectra. Bacteria at the edge of the small field of view by the camera are often segmented by the field of view. Resulting in the same bacterium being scanned up to four times, or even removed as impurities because the segmented area is too small, which can lead to loss of bacteria or repeated measurement of a certain bacterium. When each field of view is collected, the position of the bacteria cannot be automatically positioned, and only by manual selection. The traditional method [19] can only scan a single field of view to identify bacteria, and it is necessary to manually select the bacteria to be tested. If there are too many fields of view, it will increase the volume of the experiment, the operation is cumbersome, and the efficiency will be reduced. In addition, the existing Raman spectrum preprocessing methods mainly include two functions: filtering and baseline correction. Since each parameter in the algorithm has different effects on performance, the parameters need to be adjusted manually. After the Raman spectrum is collected, the traditional peak-seeking method is to find the peak manually or through third-party software, which cannot realize the whole automated process.

In this paper, we used the single-cell Raman heavy water isotope labeling technology and introduced an image stitching algorithm and automatic recognition algorithm, which can automatically calculate the number of fields to be spliced based on the set number of single cells, effectively avoiding redundant splicing and improving the efficiency of splicing and recognition, so as to realize fully automated image stitching and single cell recognition. Moreover, in the peak-seeking part of the Raman spectrum, the adaptive iteratively reweighted Penalized Least Squares (airPLS) algorithm and the peak-finding algorithm are added to achieve precise positioning of the Raman spectrum fingerprint, as well as rapid identification of the Raman spectrum within the range of 2030–2400 cm^{-1} whether there is a C-D peak, realized the fully automated analysis of the Raman spectrum of all bacteria in the sample. The research method in this article has achieved high-throughput identification of single cells and the acquisition of Raman spectra, making the experimental results more reliable and achieving unattended automatic identification process of bacterial antimicrobial resistance.

2. Materials and Methods

2.1 Sample Preparation

Two pathogenic bacteria were selected for this study, including *Klebsiella pneumoniae* and *Staphylococcus aureus*. Among them, *Klebsiella pneumoniae* included meropenem-resistant strains (minimum inhibitory concentration (MIC) = 8) and sensitive strains, and *Staphylococcus aureus* was a sensitive strain.

2.1.1 Microbial Cultivation

Configure Luria-Bertani (LB) liquid medium with a 30% concentration of heavy water (Sigma-Aldrich). The *Klebsiella pneumoniae* resistant strains and *Klebsiella pneumoniae* sensitive strains were cultured in a 30% heavy water medium, in which the antibiotic meropenem was added at a concentration of 8 μg/μL and cultured overnight at 37 °C. *Staphylococcus aureus* was cultured using LB medium and culture at 37 °C overnight.

2.1.2 Sample Handling

① Take 1 mL each of *Klebsiella pneumoniae* and *Staphylococcus aureus* cultured overnight, and centrifuge at 9000 rpm for 2 min to collect the bacterial sediment, and then use sterile water to wash the bacterial sediment three times, each time at 9000 rpm for 2 min, and finally dissolve the bacterial sediment in 1 mL of sterile water, shake and mix well. Take 100 μL of two groups of samples and shake and mix to prepare a mixed sample. 2 μL of the pure samples of *Klebsiella pneumoniae* and *Staphylococcus aureus* and the mixed samples of the two groups were spotted on the Raman chip (Champion Optics, Changchun, Jilin, China), respectively, and air-dried for Raman detection.

② Take 1 mL each of *Klebsiella pneumoniae* resistant strains and *Klebsiella pneumoniae* sensitive strains cultured overnight, the treatment conditions are the same as above, and the mixed sample is prepared. 2 μL of the pure sam-

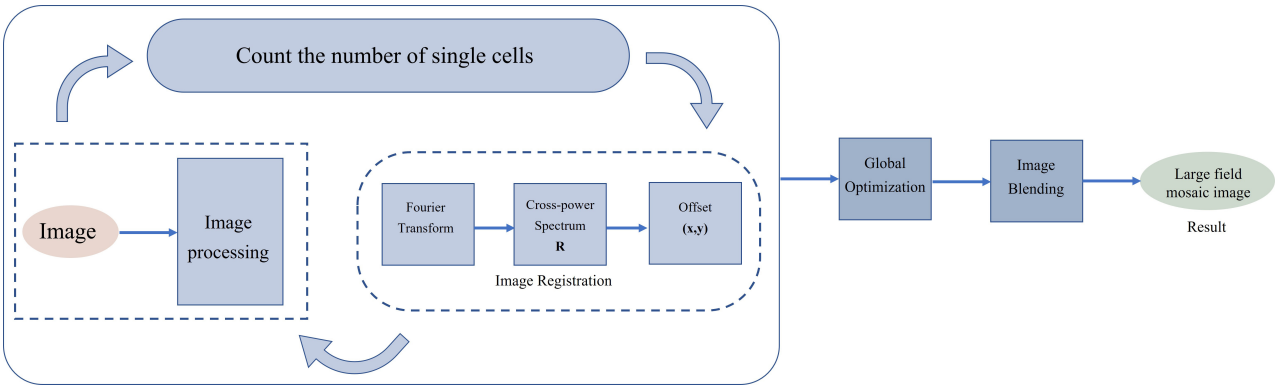

Fig. 1. Multiple fields of view image stitching flowchart.

ples of *Klebsiella pneumoniae* resistant strains and *Klebsiella pneumoniae* sensitive strains and the mixed samples of the two groups were spotted on the Raman chip, respectively, and air-dried for Raman detection.

2.2 Image Stitching

The purpose of image stitching is to automatically calculate the number of fields of view needed by scanning small fields of view with the number of bacteria entered by the user, and to stitch these overlapping small field of view images into one multiple fields of view image to obtain a panoramic image with enough bacteria. Image stitching mainly includes four stages: image identification, image registration, global optimization, and image blending. To realize the automatic calculation of the number of visual fields to be spliced to improve efficiency, the method adopted in this paper is to calculate the final number of visual fields to be spliced by the number of bacteria to be tested input by the user. The flow chart of image stitching is shown in Fig. 1.

2.2.1 Image Identification

In order to automatically calculate the number of stitched images, image recognition is performed at the same time as the acquisition of small field of view images. The number of identified bacteria in the unoverlapped area of the acquired image is accumulated and compared with the number of bacteria that the user has set to be detected to determine whether to continue acquiring images. To ensure the number of bacteria after splicing, if the accumulated bacteria do not reach the user-set number after scanning a certain line, all bacteria in the next line will be directly scanned.

Filtering and binarization of the acquired small-field images, use the *FindContours()* function of the OpenCV library to roughly calculate the number of single cells based on the size of the contours found. $n_i$denotes the number of single cells identified in the unoverlapped area of the i-th small-field image acquired, $n$denotes the number of single cells that the user wants to detect. Stop capturing images when $\sum n_i \geq n$.

2.2.2 Image Registration

Finding the spatial mapping link between the pixels of one picture and the pixels of another image and aligning them spatially with the least amount of error is known as image registration. To determine the offset between each field of view, a phase-correlation method is used. The phase correlation technology is based on the Fourier transform search concept. The offset is determined using the cross-power spectrum when there is just a translation between the two pictures. The position of the largest peak in the cross-power spectrum is the relative translation of the two images [20–23].

Let $f_1\,(x,\ y)$ and $f_2\,(x,\ y)$ be two images, they have offsets in both the x- and y-axes, as shown in Fig. 2A. $f_1$and f_2 are related by the following transformation:

$$f_2(x, y) = f_1\,(x - x_0, y - y_0) \tag{1}$$

Taking the Fourier transform of both yields the following connection, according to the shift theorem:

$$\mathrm{F}_2(\mathrm{u}, \mathrm{v}) = \mathrm{F}_1(\mathrm{u}, \mathrm{v}) * \mathrm{e}^{-\mathrm{i}*2\pi*(\mathrm{u}^*\mathrm{x}_0+\mathrm{v}*\mathrm{y}_0)} \tag{2}$$

The following is the definition of the cross-power spectrum between f_1 and f_2:

$$\mathrm{R} = \frac{\mathrm{F}_1(\mathrm{u}, \mathrm{v}) *\ \mathrm{F}_2^*(\mathrm{u}, \mathrm{v})}{|\mathrm{F}_1(\mathrm{u}, \mathrm{v}) *\ \mathrm{F}_2^*(\mathrm{u}, \mathrm{v})|} = \mathrm{e}^{-\mathrm{i}*2\pi*(\mathrm{u}*\mathrm{x}_0+\mathrm{v}*\mathrm{y}_0)} \tag{3}$$

* Denotes complicated conjugation. Applying the inverse Fourier transform to formula (3) yields the Dirac function (impulse function) $r = \mathrm{F}^{-1}\{R\}$, as illustrated in Fig. 2B. This function has a clear, sharp peak at the offset point. This function has a clear, sharp peak at the offset point, while the value at other locations is very near zero. By checking for the pulse function's peak coordinates, the offset may be discovered:

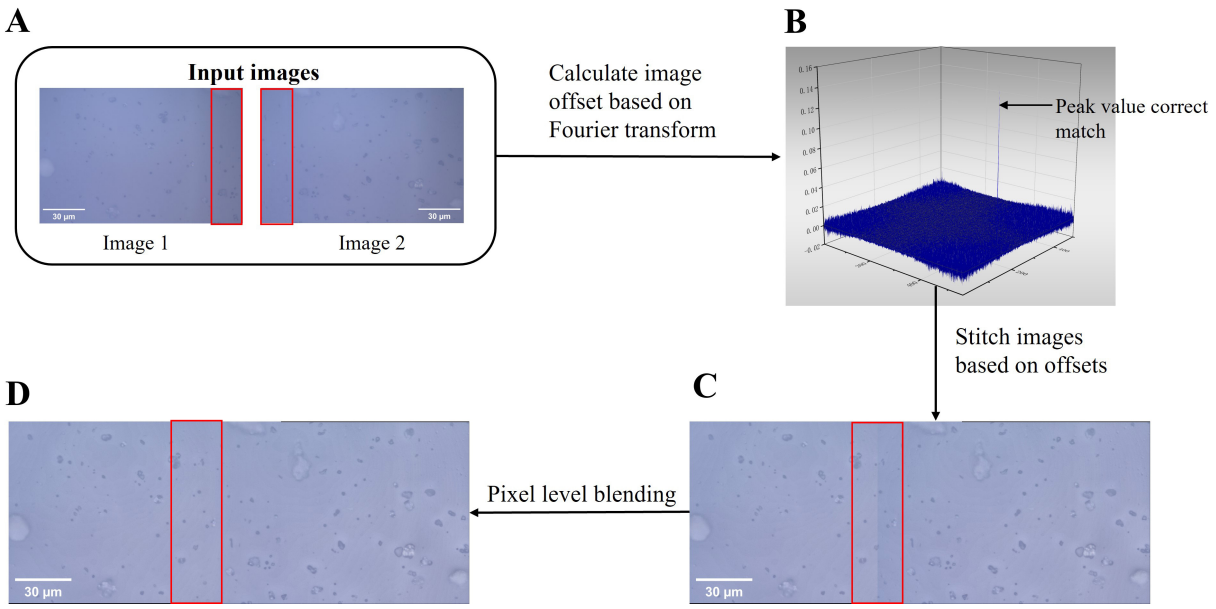

Fig. 2. Schematic diagram of fusion of two images. (A) Input two images with overlapping areas. (B) The impulse function picture was computed from the two photographs. (C) Direct stitching. Stitching seams frequently show up in panoramic stitched photos because of the associated changes in ambient light and cameras. (D) Pixel-level blending. Following pixel-level fusion processing, the stitching seams can be efficiently eliminated.

$$(\Delta x, \Delta y) = \left(\frac{1}{2}\right) \text{center}(x, y) - \underset{(x,y)}{\text{argmax}}\{r\} \quad (4)$$

2.2.3 Global Optimization

Global optimization is necessary to filter out any paired registrations that do not fit into the remainder of the connection network, identify the consistency across all pairs, and decrease errors since there are inconsistencies between the computed image offsets [24]. Fit the displacement connection of the other fields of view concerning the reference field of view using the least squares approach [25]. There is a set of transformations P = ($\vec{P}_{\text{MN}}$: M, N$\in$ V) where V is the set of all tiles, and each tile $\vec{P}_{\text{MN}}$ translates tile M to overlapping tile N, increasing pairwise alignment quality to the greatest extent possible. Given that F$\in$ V is the defined public reference horizon, the optimal configuration is defined as $Q_{\text{VF}} = \{\vec{q}_{\text{MF}} : M, \ F \in V\}$, which satisfies the following conditions:

$$\arg \min_{Q_{VF}} \sum_{\text{M}\in V\setminus\{\text{F}\}} \left(\sum_{\text{N}\in V\setminus\{\text{M}\}} \left\| \vec{q}_{NF} - \vec{q}_{MF} - \vec{P}_{MN} \right\|^2 \right) \quad (5)$$

2.2.4 Image Blending

In general, the overlapping portions will exhibit variances in light and dark intensity and degree of distortion due to the difference in sample time and sampling angle between the two pictures, and there will unavoidably be seams along the edge of the stitching. Therefore, it is necessary to add an illumination compensation algorithm to remove dark corners from the image: divide an image into M $\times$ N small blocks, calculate the average gray level of each small block, obtain the brightness matrix A of the small block, subtract the average gray level of the image from A, and obtain the average gray level of the small block Brightness difference matrix B. Through interpolation, matrix B is interpolated to matrix C with the same size as the original image, and the corrected image is obtained after subtracting matrix C from the gray value of the original image [26].

Above all, it is required to apply a smooth transition fusion procedure to the image to make the spliced image appear to have no seams [24,27–29]. Linear fusion of the pixels in the overlapped area is the fusion technique employed in this work (Fig. 2C). By using linear blending, the weight of the pixels in the overlapped region is determined using the contribution block T_i's weighting factor at each point [30]. The closer the pixel l_i in the overlapping region is to the image boundary, the less it contributes to the overall intensity, dim refers to the dimension, representing the horizontal direction and the vertical direction. $l_{i,dim}$means that the coordinates of the pixel are extracted into two components in the horizontal direction and the vertical direction. Similarly, $T_{i,dim}$represents the length and width of the image block as two components in the horizontal direction and vertical direction, so that the shortest distance between l_i and the horizontal boundary and vertical boundary of the image can be calculated respectively. The final fusion effect is shown in Fig. 2D.

The following formula defines the separation between each pixel and the picture border:

$$d_{i,dim}^{\min} = \min\left(l_{i,dim}, \text{size}\left(T_{i,dim} - l_{i,dim}\right)\right) \quad (6)$$

T_i is a block of images. This pixel is simultaneously located in the region where n fields of view overlap. Initial weighting factor $v(T_i) = \prod_{dim} d_{i,dim}^{min} / \sum_i^n \prod_{dim} d_{i,dim}^{min}$, the following is the final weight $w(T_i)$formula, the parameter αcontrols how the overlapping sections are blended:

$$\mathrm{w}\left(\mathrm{T_i}\right) = \left(\sum\nolimits_{\mathrm{j}} \mathrm{v}\left(\mathrm{T_j}\right) - \sum\nolimits_{\mathrm{k}\neq\mathrm{i}} \mathrm{v}\left(\mathrm{T_k}\right)\right)^{\alpha} \text{ and } \sum\nolimits_{\mathrm{i}} \mathrm{w}\left(\mathrm{T_i}\right) = 1 \quad (7)$$

2.3 Identification and Localization of Bacteria

There are 6 steps to identify and locate single cells and excluded the impurities and cluster phenomena. Fig. 3E, F in the image after stitching scanning areas: (1) Preprocess the input image: The colorful image should be transformed into a gray image; use a filter to reduce noise on the gray image (Fig. 3A). (2) The gray image reduced noise should be transformed into multiple binary images by increasing from the minimum threshold to the maximum threshold by threshold step. Fig. 3B shows one of the binary images. (3) Use the *FindContours()* function of the OpenCV library (Open Source Computer Vision Library) [31] to detect the blobs of the binary images (Fig. 3C) [32]. (4) The blob center coordinates of binary images are grouped by the minimum distance between connected components. From each group, estimate the final center of the blobs and their radius, and return the location and area of the points (Fig. 3D). (5) Filter the returned blobs with the following characteristics: Area; roundness calculated by $C = \frac{4\Pi S}{P^2}$ (C approaches 1, the blob is perfectly circular; C approaches 0, the blob is a polygon close to a straight line; C is between 0.75~0.85, the blob is an equilateral polygon); eccentricity calculated by $E^2 + I^2 = 1$ (I approaches 1, the blob is perfectly circular; I approaches 0, the blob is a polygon close to a straight line; I is between 0~1, the blob is an ellipse); convexity indicates whether the geometry is a convex polygon or a concave polygon calculated by $V = \frac{S}{H}$ (V is between 0~1; V >0.5, blob approaches a circular). We number the identified bacteria to quickly and accurately locate them and provide assistance in verifying their Raman spectra if necessary. Fig. 3E,F shows the screening of single cells in a small field of view with excessive cluster phenomena and in a small field of view with too few single cells, respectively. Impurities and cluster phenomena are excluded. Due to the obvious difference between the peak position of the Raman spectrum of the biological sample and the peak position of the cluster phenomenon, therefore, impurities and cluster phenomena are excluded (**Supplementary Figs. 1,2**).

By analyzing the antibiotic resistance of 2530 sensitive bacteria (*Staphylococcus aureus*) and 2224 resistant bacteria (*Klebsiella pneumoniae*) in experiment 1, respectively (Table 1), we evaluated the accuracy of identifying bacterial resistance (in %) derived from the ratio of the number of bacteria with correct identification of resistance to the total number of bacteria detected.

2.4 Automatic Collection of Raman Spectrum

Raman Spectra from microorganisms were acquired with the confocal Raman spectrometer HOOKE R300 (Hooke Instrument Ltd., Changchun, Jilin, China) and HOOKE P300 (Hooke Instrument Ltd., Changchun, Jilin, China) for experiment 1 and experiment 2, respectively. Diffraction gratings with groove densities of 600 g/mm (spectral resolutions of 3–4 cm^{-1}) and a charge coupled device (CCD) camera (1340 × 100 pixel, PIXIS 100B, Princeton Instrument (PI)) are used for the field-by-field automatic scanning. The 100× objective lenses generate a diffraction-limited spot size, ~1 μm in diameter. The scanning wave number range is 340–3750 cm^{-1} (600 g/mm diffraction grating).

Identify and locate single cells on multiple fields of view image after stitching 9 × 11 and 11 × 11 scanning areas for experiment 1 and experiment 2, respectively, the coordinates of center points of the single cells were communicated to the motorized stage, then, laser emitted from a solid-state laser (08-DPL, Cobolt, Sweden) with a wavelength of 532 nm was focused on the bacterial centroid at 5 mw/3 s by moving the motorized stage to excite the Raman signal. Finally, the Raman Spectra of bacteria are obtained. We collected 2706 and 2048 Raman Spectra for experiment 1 and experiment 2, respectively.

2.5 Raman Spectra Processing and Peak Searching

In order to reduce the initial Raman Spectrum burr caused by signal jitter and other factors, the Savitzky-Golay (SG) filtering method [33,34] is used to wight filter the Raman Spectrum to obtain smooth signal change information (Fig. 4A).

To eliminate the background noise, we calibrate the baseline of the smoothed Raman Spectrum using an adaptive iteratively reweighted Penalized Least Squares (airPLS) algorithm [35,36] (Fig. 4A). Adaptive iteratively reweighted Penalized Least Squares (airPLS) algorithm doesn't require any user intervention and prior information, such as detected peaks. It iteratively changes weights of sum squares errors (SSE) between the fitted baseline and original signals, and the weights of SSE are obtained adaptively using previously fitted baseline and original signals. This baseline estimator is fast and flexible in fitting the baseline [37].

Automatic peaking of Raman spectra using Persistence1D to extract [38], pair, and sorted local minima and local maxima according to their persistence (Fig. 4B). Scan and save the Raman spectrum of each bacterium in the sam-

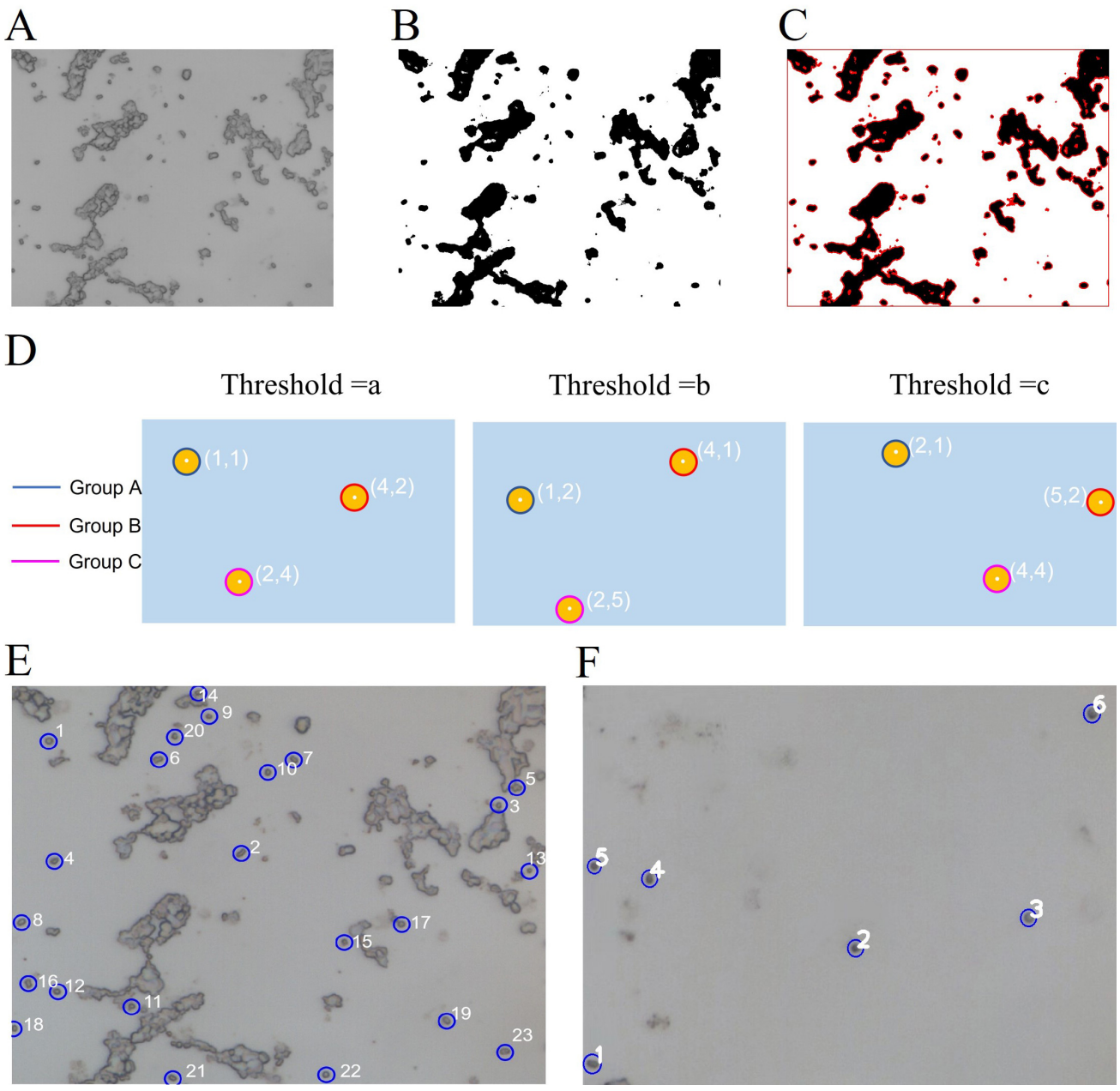

Fig. 3. Schematic diagram of image recognition. (A) Pre-processed gray image. (B) One of the binary images. (C) Use the *FindContours()* function to detect the contours of (B). (D) The contours detected in multiple binary images are grouped according to the coordinates of their center points. (E) Screening single cells in a small field of view with excessive cluster phenomena. (F) Screening single cells in a small field of view with too few single cells.

ple, then analyze antibiotic resistance by Automatic peaking Raman Spectroscopy. Therefore, a completely automated process is realized.

3. Results and Discussion

3.1 Stitching Small Field of View Images

For experiment 1, the number of bacteria set by the user is 2500, and the actual number of collected bacteria is 2706. 9 × 11 scanning areas of 118.5 × 79 μm under 100 × objective lenses (Nikon, Tokyo, Japan) collected by Raman spectrometer HOOKE R300 (Hooke Instrument Ltd., China) were stitched. Each 118.5 × 79 μm scanning area overlaps its adjacent scanning areas by 20%. Fig. 5A shows the 880.6 × 711.9 μm (22,826 × 18,453 pixels) multiple fields of view image after stitching 9 × 11 scanning areas of 118.5 × 79 μm (3072 × 2048 pixels).

For experiment 2, the number of bacteria set by the user is 2000, and the actual number of collected bacteria is 2048. 11 × 11 scanning areas of 88.5 × 70.8 μm (1280 × 1024 pixels) under 100 × objective lenses (Olympus,

Table 1. The number of antibiotic-resistant bacteria and antibiotic-sensitive bacteria were identified and the calculation of accuracy, precision, and recall.

Predicted	Actual		Total
	Bacteria with a heavy water (antibiotic-resistant bacteria)	Bacteria without a heavy water (antibiotic-sensitive bacteria)	
Bacteria with a heavy water (antibiotic-resistant bacteria)	TP (2216)	FP (8)	2224
Bacteria without a heavy water (antibiotic-sensitive bacteria)	FN (2)	TN (2528)	2530
Total	2218	2536	4754
Accuracy = (TP + TN) / (TP + TN + FP + FN) = 0.998			
Precision = TP / (TP + FP) = 0.996			
Recall = TP / (TP + FN) = 0.999			

TP, it is predicted that bacteria with C-D peak have a C-D peak; FP, the bacteria predicted to have a C-D peak have no C-D peak; FN, it is predicted that bacteria without C-D peak have a C-D peak; TN, it is predicted that bacteria with no C-D peak have no C-D peak.

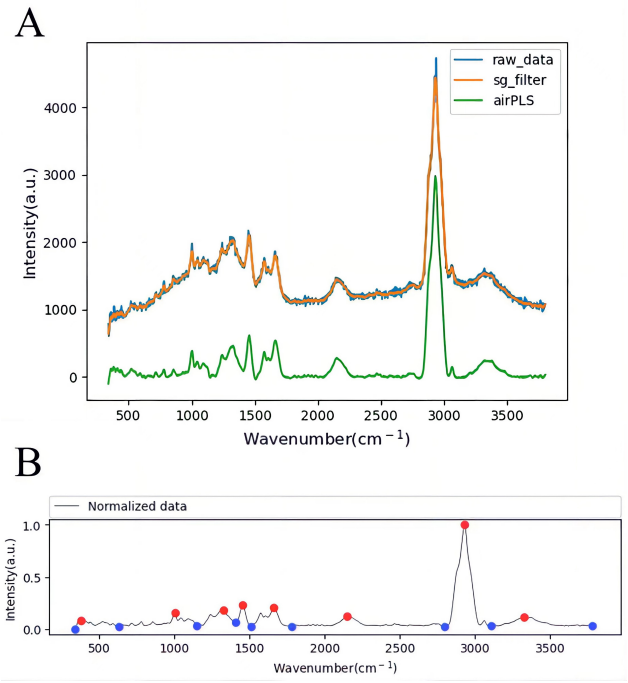

Fig. 4. Raman Spectrum pretreatment and peak searching. (A) Raman Spectrum pretreatment with SG filter and adaptive iteratively reweighted Penalized Least Squares (airPLS). (B) Raman Spectrum peak searching.

Tokyo, Japan) collected by Raman spectrometer HOOKE P300 (Hooke Instrument Ltd., China) were stitched to a 799.8 × 637.5 µm (11,565 × 9218 pixels) multiple fields of view image (Fig. 5B). Each 88.5 × 70.8 µm scanning area overlaps its adjacent scanning areas by 20%.

For both multiple fields of view images, the illumination compensation algorithm is used to reduce the dark corners around the image. In image registration, the error caused by redundant information was reduced because only phase correlation is used for overlapping areas. Stitching accomplished without losing information based on the prior knowledge of the offset of the shift table.

3.2 Differences in Raman Spectra between Sensitive and Resistant Bacteria

Numerous studies have reported that there are differences in molecular structure between antibiotic-resistant bacteria and sensitive bacteria [39,40]. By collecting Raman Spectra of bacteria and determining whether there is a C-D peak, antibiotic-resistant bacteria and sensitive bacteria can be quickly distinguished. In this study, we analyze whether the Raman Spectra of bacteria have a peak in the wave number range of 2040–2300 cm^{-1} to distinguish whether they are antibiotic-resistant bacteria.

Fig. 5C,D shows the Raman Spectra images of antibiotic-resistant bacteria and sensitive bacteria from experiment 1 and experiment 2, respectively. The comparison shows that the C-D characteristic peak appeared in the range of Raman Spectra wave number 2040–2300 cm^{-1} for antibiotic-resistant bacteria. It shows that the H+/D+ exchange reaction based on nicotinamide adenine dinucleotide phosphate (NADPH) is carried out synchronously in the denitrification process [41–43], and doped with deuterium from D_2O, it is related to the metabolic activity of bacteria. The sensitive bacteria have lost their activity due to soaking by antibiotics, therefore, when sensitive bacteria were labeled with heavy water, there was no C-D peak in Raman Spectra because they did not react with deuterium.

3.3 Number of Antibiotic Resistant Bacteria and Sensitive Bacteria

Whether the bacteria are antibiotic resistant can be identified by the presence of a C-D peak in the range of 2040–2300 cm^{-1}, when there is a C-D peak, the bacteria are antibiotic-resistant bacteria, and when there is no C-D peak, the bacteria are antibiotic-sensitive bacteria [44,45]. After Raman Spectra analysis of the bacteria, the contours

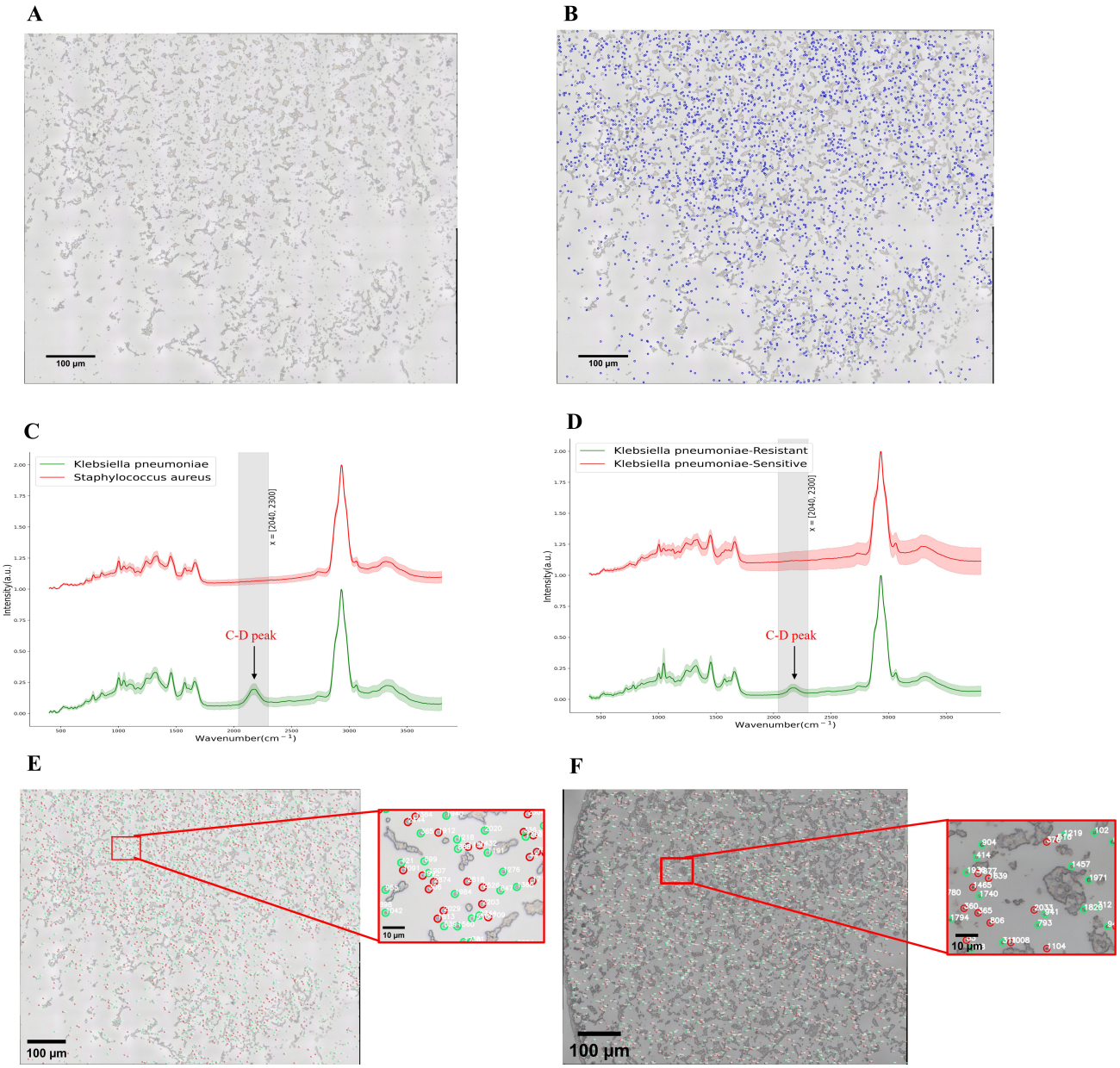

Fig. 5. The conclusion diagram following data processing. (A) Multiple fields of view image after stitching 9 × 11 scanning areas in experiment 1. (B) Identifies all single cells in (A). Impurities and cluster phenomena are excluded. (C) Statistical analysis image of Raman Spectra average of *Staphylococcus aureus* and *Klebsiella pneumoniae* in experiment 1. Red represents the Raman spectrum of *Klebsiella pneumoniae* in medium with heavy water, there is a C-D peak in the range of 2040–2300 cm^{-1}. For antibiotic-resistant and sensitive bacteria, 1137 and 1569 Raman spectra were collected for statistical analysis respectively. (D) Statistical analysis image of Raman Spectra average of *Klebsiella pneumoniae* sensitive bacteria and *Klebsiella pneumoniae* antibiotic-resistant bacteria in experiment 2. Red represents the Raman spectrum of *Klebsiella pneumoniae* antibiotic-resistant bacteria in medium with heavy water, there is a C-D peak in the range of 2040–2300 cm^{-1}. For antibiotic-resistant and sensitive bacteria, 1087 and 961 Raman spectra were collected for statistical analysis respectively. (E,F) Distribution of antibiotic-resistant bacteria and sensitive bacteria in multiple fields of view image and its partially enlarged detail. Antibiotic-resistant bacteria are drawn in green; Sensitive bacteria are drawn in red.

and centroids were plotted for antibiotic-resistant bacteria and sensitive bacteria using different colors.

Table 1 shows that the number of bacteria with a C-D peak detected in 2224 antibiotic-resistant bacteria is 2216; The number of bacteria without a C-D peak detected in 2224 antibiotic-resistant bacteria is 8; The number of bacteria without a C-D peak detected in 2530 antibiotic-sensitive bacteria is 2528; The number of bacteria with a C-D peak detected in 2530 antibiotic-sensitive bacteria is 2. The results showed that the accuracy of identifying was 99.8%

which used rapid detection and analysis of Raman Spectra of bacteria in multiple fields of view based on an image stitching technique. Experiment 1 shows that the number of antibiotic-resistant bacteria was 1137, accounting for 42%; The number of sensitive bacteria was 1569, accounting for 58%. Experiment 2 shows that the number of antibiotic-resistant bacteria was 1087, accounting for 53%; The number of sensitive bacteria was 961, accounting for 47%.

Fig. 5E,F shows the distribution of antibiotic-resistant bacteria and sensitive bacteria in experiment 1 and experiment 2, respectively.

4. Conclusions

To achieve high throughput, rapid and accurate detection of antimicrobial-resistance by Raman spectroscopy, we have proposed rapid detection and analysis of Raman Spectra of bacteria in multiple fields of view based on an image stitching technique. The method researched in this paper focuses on single-cell Raman spectra, combined with isotope labeling, and integrates multiple algorithms for optimization to automatically calculate of the number of stitched small fields of view by the number of bacteria entered by the user and determine the presence or absence of peaks in a set peak interval to achieve unattended, automated identification of bacterial antimicrobial resistance. Currently available products, such as the ParticleScout program and Fiji, there is no doubt that they are very mature software at present. In the part of image stitching, both of them can perform accurate and seamless stitching according to the set stitching range, and Particlescout can be used in environmental science, food technology, and other fields. Carry out localization and classification, and further study the samples by confocal Raman imaging. The method studied in this paper is mainly applied to the biomedical field. According to the number of single cells to be identified entered by the user, the range of image stitching is automatically calculated. Combined with heavy water labeling and Raman spectroscopy, the whole process of automatic and unsupervised analysis of single-cell antibiotic resistance in antibiotic sensitivity tests is realized in multiple fields of view. Then we have calculated the accuracy of this method. The automatically analyze bacteria Raman spectra method in multiple fields of view can accurately identify single cells and accurately identify bacterial antibiotic resistance (The accuracy rate is 99.8%). The results indicate that the automatically analyze bacteria Raman spectra method in multiple fields of view can rapidly and accurately analyze antimicrobial resistance. As a result, the automatically analyze bacteria Raman spectra method in multiple fields of view can be used as a high-throughput, rapid and accurate method to detect antimicrobial resistance by Raman spectroscopy for researching the persistence and spread of antibiotics in bacterial pathogens, which will benefit the medical field and microbiology field.

Availability of Data and Materials

The authors are unable or have chosen not to specify which data has been used. The data used in this study is for commercial use and readers may contact the corresponding author if they would like this data.

Author Contributions

XD and FY designed the study, wrote the software, collected the data, and wrote the manuscript. YX prepared samples. NW analyzed data. HH participated in the analysis of the data as well as the revision of the manuscript. BL contributed to experimental design and manuscript revisions. All authors contributed to editorial changes in the manuscript. All authors read and approved the final manuscript. All authors have participated sufficiently in the work and agreed to be accountable for all aspects of the work.

Ethics Approval and Consent to Participate

Not applicable.

Acknowledgment

We would like to thank the study participants for actively participating. Thanks for the support of the bacterial drug resistance rapid detection instrument based on Raman technology project.

Funding

This study was supported by the bacterial drug resistance rapid detection instrument based on Raman technology project (grant no. 20190302015GX).

Conflict of Interest

Given his role as Guest Editor, Bei Li had no involvement in the peer-review of this article and has no access to information regarding its peer-review. Full responsibility for the editorial process for this article was delegated to Josef Jampílek. The authors declare no conflict of interest.

Supplementary Material

Supplementary material associated with this article can be found, in the online version, at https://doi.org/10.31083/j.fbl2810249.

References

[1] Verma T, Annappa H, Singh S, Umapathy S, Nandi D. Profiling antibiotic resistance in Escherichia coli strains displaying differential antibiotic susceptibilities using Raman spectroscopy. Journal of Biophotonics. 2021; 14: e202000231.

[2] McAdams D. Resistance diagnosis and the changing epidemiology of antibiotic resistance. Annals of the New York Academy of Sciences. 2017; 1388: 5–17.

[3] Germond A, Ichimura T, Horinouchi T, Fujita H, Furusawa C, Watanabe TM. Raman spectral signature reflects transcriptomic

features of antibiotic resistance in *Escherichia coli*. Communications Biology. 2018; 1: 85.
[4] Antimicrobial Resistance Collaborators. Global burden of bacterial antimicrobial resistance in 2019: a systematic analysis. Lancet. 2022; 399: 629–655.
[5] Kurt Yilmaz N, Schiffer CA. Introduction: Drug Resistance. Chemical Reviews. 2021; 121: 3235–3237.
[6] Yi X, Song Y, Xu X, Peng D, Wang J, Qie X, *et al*. Development of a Fast Raman-Assisted Antibiotic Susceptibility Test (FRAST) for the Antibiotic Resistance Analysis of Clinical Urine and Blood Samples. Analytical Chemistry. 2021; 93: 5098–5106.
[7] Bi L, Wang X, Cao X, Liu L, Bai C, Zheng Q, *et al*. SERS-active Au@ Ag core-shell nanorod (Au@ AgNR) tags for ultrasensitive bacteria detection and antibiotic-susceptibility testing. Talanta. 2020; 220: 121397.
[8] March-Rosselló GA. Rapid methods for detection of bacterial resistance to antibiotics. Enfermedades Infecciosas Y Microbiologia Clinica. 2017; 35: 182–188.
[9] Chen L, Wang X. Molecular mechanism of bacterial drug resistance based on embedded system and rapid detection method of drug resistance gene. Microprocessors and Microsystems. 2021; 82: 103912.
[10] Hanlon EB, Manoharan R, Koo TW, Shafer KE, Motz JT, Fitzmaurice M, *et al*. Prospects for *in vivo* Raman spectroscopy. Physics in Medicine and Biology. 2000; 45: R1.
[11] Eberhardt K, Stiebing C, Matthäus C, Schmitt M, Popp J. Advantages and limitations of Raman spectroscopy for molecular diagnostics: an update. Expert Review of Molecular Diagnostics. 2015; 15: 773–787.
[12] Boardman AK, Wong WS, Premasiri WR, Ziegler LD, Lee JC, Miljkovic M, *et al*. Rapid Detection of Bacteria from Blood with Surface-Enhanced Raman Spectroscopy. Analytical Chemistry. 2016; 88: 8026–8035.
[13] Wang C, Chen R, Xu J, Jin L. Single-cell Raman spectroscopy identifies *Escherichia coli* persisters and reveals their enhanced metabolic activities. Frontiers in Microbiology. 2022; 13: 936726.
[14] Thomsen BL, Christensen JB, Rodenko O, Usenov I, Grønnemose RB, Andersen TE, *et al*. Accurate and fast identification of minimally prepared bacteria phenotypes using Raman spectroscopy assisted by machine learning. Scientific Reports. 2022; 12: 16436.
[15] Taubert M, Stöckel S, Geesink P, Girnus S, Jehmlich N, von Bergen M, *et al*. Tracking active groundwater microbes with D_2 O labelling to understand their ecosystem function. Environmental Microbiology. 2018; 20: 369–384.
[16] Feng J, Yao W, Guo Y, Cheng Y, Qian H, Xie Y. Incorporation of Heavy Water for Rapid Detection of Salmonella typhimurium by Raman Microspectroscopy. Food Analytical Methods. 2018; 11: 3551–3557.
[17] Zhang P, Wu XH, Su L, Wang HQ, Lin TF, Fang YP, *et al*. Rapid, Label-Free Prediction of Antibiotic Resistance in *Salmonella typhimurium* by Surface-Enhanced Raman Spectroscopy. International Journal of Molecular Sciences. 2022; 23: 1356.
[18] Yang K, Li HZ, Zhu X, Su JQ, Ren B, Zhu YG, *et al*. Rapid Antibiotic Susceptibility Testing of Pathogenic Bacteria Using Heavy-Water-Labeled Single-Cell Raman Spectroscopy in Clinical Samples. Analytical Chemistry. 2019; 91: 6296–6303.
[19] Wang Y, Peng H, Liu K, Shang L, Xu L, Lu Z, *et al*. Multi-point scanning confocal Raman spectroscopy for accurate identification of microorganisms at the single-cell level. Talanta. 2023; 254: 124112.
[20] Kuglin CD. The phase correlation image alignment method. Proc. Int. Conf. Cybernetics Society. San Francisco, USA, Jan. 1975; 163–165.
[21] Samritjiarapon O, Chitsobhuk O. An FFT-Based technique and best-first search for image registration. 2008 International Symposium on Communications and Information Technologies. Institute of Electrical and Electronics Engineers. Vientiane, Laos, October. 2008; 364–367.
[22] Druckmüller M. Phase correlation method for the alignment of total solar eclipse images. The Astrophysical Journal. 2009; 706: 1605–1608.
[23] Konstantinidis D, Stathaki T, Argyriou V. Phase Amplified Correlation for Improved Sub-pixel Motion Estimation. IEEE Transactions on Image Processing. 2019; 28: 3089–3101.
[24] Fang F, Wang T, Fang Y, Zhang G. Fast color blending for seamless image stitching. IEEE Geoscience and Remote Sensing Letters. 2019; 16: 1115–1119.
[25] Preibisch S, Saalfeld S, Tomancak P. Globally optimal stitching of tiled 3D microscopic image acquisitions. Bioinformatics. 2009; 25: 1463–1465.
[26] Kim TS, Kim SH. An improved contrast enhancement for dark images with non-uniform illumination based on edge preservation. Multimedia Systems. 2022; 29: 1117–1130.
[27] Pellikka M, Lahtinen V. A robust method for image stitching. Pattern Analysis and Applications. 2021; 24: 1847–1858.
[28] Song B. Optimization of the Progressive Image Mosaicing Algorithm in Fine Art Image Fusion for Virtual Reality. IEEE Access. 2020; 9: 69559–69572.
[29] Chen M, Zhao X, Xu D. Image Stitching and Blending of Dunhuang Murals Based on Image Pyramid. Journal of Physics. 2019; 1335: 012024.
[30] Preibisch S, Saalfeld S, Tomancak P. Fast stitching of large 3d biological datasets. Proceedings of the 2nd ImageJ User and Developer Conference. Luxembourg. 2008; 7–8.
[31] Open Computer Vision Library [Electronic resource]. 2012. Available at: http://sourceforge.net/projects/opencvlibrary (Accessed: 25 June 2012).
[32] Suzuki S. Topological structural analysis of digitized binary images by border following. Computer vision, graphics, and image processing. 1985; 30: 32–46.
[33] Člupek M, Matějka P, Volka K. Noise reduction in Raman spectra: Finite impulse response filtration versus Savitzky–Golay smoothing. Journal of Raman Spectroscopy. 2007; 38: 1174–1179.
[34] Huang J, Shi T, Gong B, Li X, Liao G, Tang Z. Fitting an Optical Fiber Background with a Weighted Savitzky-Golay Smoothing Filter for Raman Spectroscopy. Applied Spectroscopy. 2018; 72: 1632–1644.
[35] Guo S, Bocklitz T, Popp J. Optimization of Raman-spectrum baseline correction in biological application. Analyst. 2016; 141: 2396–2404.
[36] Tsuyama S, Taketani A, Murakami T, Sakashita M, Miyajima S, Ogawa T, *et al*. Quantitative prediction of a functional ingredient in apple using Raman spectroscopy and multivariate calibration analysis. Applied Physics B. 2021; 127: 1–7.
[37] Mikhailyuk IK, Razzhivin AP. Background subtraction in experimental data arrays illustrated by the example of Raman spectra and fluorescent gel electrophoresis patterns. Instruments and Experimental Techniques. 2003; 46: 765–769.
[38] Weinkauf T, Günther D. Separatrix Persistence: Extraction of Salient Edges on Surfaces Using Topological Methods. Computer Graphics Forum. 2009; 28: 1519–1528.
[39] Moradi H, Ahmad A, Shepherdson D, Vuong NH, Niedbala G, Eapen L, *et al*. Raman micro-spectroscopy applied to treatment resistant and sensitive human ovarian cancer cells. Journal of Biophotonics. 2017; 10: 1327–1334.
[40] Stöckel S, Kirchhoff J, Neugebauer U, Rösch P, Popp J. The application of Raman spectroscopy for the detection and iden-

tification of microorganisms. Journal of Raman Spectroscopy. 2016; 47: 89–109.

[41] Liu Z, Xue Y, Yang C, Li B, Zhang Y. Rapid identification and drug resistance screening of respiratory pathogens based on single-cell Raman spectroscopy. Frontiers in Microbiology. 2023; 14: 1065173.

[42] Song Y, Cui L, López JÁS, Xu J, Zhu YG, Thompson IP, *et al*. Raman-Deuterium Isotope Probing for *in-situ* identification of antimicrobial resistant bacteria in Thames River. Scientific Reports. 2017; 7: 16648.

[43] Azemtsop Matanfack G, Taubert M, Guo S, Bocklitz T, Küsel K, Rösch P, *et al*. Monitoring Deuterium Uptake in Single Bacterial Cells via Two-Dimensional Raman Correlation Spectroscopy. Analytical Chemistry. 2021; 93: 7714–7723.

[44] Guo L, Ye C, Cui L, Wan K, Chen S, Zhang S, *et al*. Population and single cell metabolic activity of UV-induced VBNC bacteria determined by CTC-FCM and D_2O-labeled Raman spectroscopy. Environment International. 2019; 130: 104883.

[45] Tao Y, Wang Y, Huang S, Zhu P, Huang WE, Ling J, *et al*. Metabolic-Activity-Based Assessment of Antimicrobial Effects by D_2O-Labeled Single-Cell Raman Microspectroscopy. Analytical Chemistry. 2017; 89: 4108–4115.